ADVANCED HEALTHCARE MATERIALS
www.advhealthmat.de

Controllable Regulation of Ag_2S Quantum-Dot-Mediated Protein Nanoassemblies for Imaging-Guided Synergistic PDT/PTT/Chemotherapy against Hypoxic Tumor

Mengjie He, Ziyi Cheng, Zhenkai Wang, Min Li, Huixian Liang, Heng Liu, Lijuan Yu, Linlu Zhao,* and Fabiao Yu**

The combination of phototherapy and chemotherapy holds great potential for cancer treatment, while hypoxia in tumor as well as unexpected drug release largely restricts anticancer therapy. Inspired by the natural intelligence, herein, for the first time, a "bottom-up" protein self-assembly strategy mediated by near-infrared (NIR) quantum dots (QDs) with multicharged electrostatic interactions is presented to develop a tumor microenvironment (TME)-responsive theranostic nanoplatform for imaging-guided synergistic photodynamic therapy (PDT)/photothermal therapy (PTT)/chemotherapy. Catalase (CAT) possesses diverse surface charge distribution under different pH conditions. After modification by chlorin e6 (Ce6), the formulated CAT–Ce6 with patchy negative charges can be assembled with NIR Ag_2S QDs by regulating their electrostatic interactions, allowing for effective incorporation of specific anticancer drug oxaliplatin (Oxa). Such Ag_2S@CAT–Ce6@Oxa nanosystems are able to visualize nanoparticle (NP) accumulation to guide subsequent phototherapy, together with significant alleviation of tumor hypoxia to further enhance PDT. Moreover, the acidic TME triggers controllable disassembly through weakening the CAT surface charge to disrupt electrostatic interactions, allowing for sustained drug release. Both in vitro and in vivo results demonstrate remarkable inhibition of colorectal tumor growth with a synergistic effect. Overall, this multicharged electrostatic protein self-assembly strategy provides a versatile platform for realizing TME-specific theranostics with high efficiency and safety, promising for clinical translation.

1. Introduction

Colorectal cancer (CRC), ranking third in terms of incidence but second in terms of mortality, has become a major burden of disease worldwide.[1] Traditional therapies for CRC, such as surgery and chemotherapy, have always caused excessive damage or unavoidable side effects to the body,[1,2] with a 5 year survival rate of only 12% when CRC metastasizes to other organs.[3] Recently, photodynamic therapy (PDT), a process in which a light-activated photosensitizer (PS) produces cytotoxic reactive oxygen species to trigger cell apoptosis, has emerged as a secure and efficient modality in anticancer therapy due to its noninvasiveness, high selectivity, and minimal side effects.[4–7] In particular, PDT is being tested in the clinic for the treatment of superficial tumors and has achieved remarkable results.[8] Most PSs in PDT mainly follow the oxygen-dependent type II mechanism, which is limited by oxygen supply.[4] Studies have shown that hypoxia is a hallmark of malignant tumors with the overexpression of hypoxia-inducible factor-1α (HIF-1α), which correlates with tumor metastasis and the increased mortality rate.[9] The implementation of PDT is often compromised by the hypoxic tumor microenvironment (TME) with $pO_2 \leq 2.5$ mmHg and may, in turn, exacerbate tumor hypoxia to some extent. Therefore, alleviating tumor hypoxia is crucial to effectively delay tumor progression, prevent tumor metastasis, and at the same time enhance the efficacy of PDT.[10]

Various strategies have been proposed to overcome hypoxia in tumor tissue such as direct oxygen delivery, improvement of

M. He, L. Yu, L. Zhao, F. Yu
Medical Imaging Department
Affiliated Cancer Hospital of Hainan Medical University
Hainan Medical University
Haikou 570312, China
E-mail: yulijuan2003@hainmc.edu.cn; zhaolinlu@hainmc.edu.cn; yufabiao@hainmc.edu.cn

The ORCID identification number(s) for the author(s) of this article can be found under https://doi.org/10.1002/adhm.202300752

DOI: 10.1002/adhm.202300752

M. He, Z. Cheng, Z. Wang, M. Li, H. Liang, H. Liu, L. Zhao, F. Yu
Key Laboratory of Hainan Trauma and Disaster Rescue
The First Affiliated Hospital of Hainan Medical University
Hainan Medical University
Haikou 571199, China

M. He, Z. Cheng, Z. Wang, M. Li, H. Liang, H. Liu, L. Zhao, F. Yu
Engineering Research Center for Hainan Bio-Smart Materials and Bio-Medical Devices
College of Emergency and Trauma
Hainan Medical University
Haikou 571199, China

intratumoral blood flow, and in situ oxygen generation, as well as economic methods to reduce oxygen consumption.[11–14] Considering the existence of high levels of hydrogen peroxide (H_2O_2) inside solid tumors, exploiting catalase (CAT), a specific catalytic enzyme with high efficiency, to decompose H_2O_2 into oxygen, seems to be an attractive strategy and has been successfully utilized in several types of theranostic nanosystem to relieve tumor hypoxia.[15–17] On the other hand, the isoelectric point (PI) of the biocompatible CAT is 5.8–6.4,[18,19] close to the pH of the acidic TME, which may endow it with controllable regulation ability under pathological conditions. Apart from hypoxia, another critical factor in the PDT process is finding the optimal therapeutic time window for light irradiation. Currently, the utilization of near-infrared (NIR) fluorescence imaging (650–900 nm) to guide PDT has become a prerequisite for precision medicine, mainly due to the decreased autofluorescence and deep penetration capability of NIR fluorescence, which are favorable for in vivo imaging. Especially, quantum dots (QDs) are a class of highly promising fluorophores with high quantum yields, tunable spectra, and high photostability.[20] Compared to the most studied QDs containing the toxic elements Cd, Pb, or Hg, Ag_2S QDs with negligible toxicity and excellent biocompatibility have been recognized as desirable candidates for in vivo fluorescence imaging in recent years.[21–23] Notably, NIR Ag_2S QDs also possess photothermal effect to achieve photothermal therapy (PTT).[24,25] Currently, the development direction of clinical research is moving toward combining PDT with other therapies such as chemotherapy and PTT, which has been confirmed to be more effective than single therapy.[17,26–28] However, the light-activated motif for PDT or PTT encapsulated in conventional nanocarriers may suffer from self-aggregation and premature leakage for in vivo applications, which ultimately affect the therapeutic efficacy. In addition, the hydrophobicity, systemic toxicity, and controllable release of the drugs in chemotherapy are also key challenges existed.[29] In view of this, how to orderly integrate the building block modules together to maximize their own functional advantages with high safety is a task of top priority in realizing multimodal synergistic cancer therapy.

The development of "bottom-up" self-assembly nanotechnology provides an effective means of organizing multiple components into an entire nanosystem to build highly ordered architectures.[30,31] In particular, nature has already utilized proteins as versatile building blocks to produce a dizzying array of materials via supramolecular self-assembly to perform vital functions.[32] Inspired by natural wisdom, great efforts have been made to exploit self-assembly for the construction of novel biomimetic nanomaterials.[27,33] Compared with conventional encapsulated nanocarriers, direct self-assembly of functional motifs can effectively reduce the introduction of nonfunctional molecules, further improving biosafety and increasing the potential for clinical translation.[34] Molecular self-assembly is usually mediated by weak noncovalent interactions—notably hydrophobic interactions, electrostatic interactions, hydrogen bonding, and metal–coordination interactions.[35] Among these, electrostatic interactions have widely been applied due to their excellent long-range and dynamically reversible properties.[36] However, single-charge electrostatic assemblies are usually weak and unstable, especially under complex in vivo conditions. In contrast, multicharge-driven electrostatic assembly not only preserves the dynamic controllability of the supramolecular assembly, but also maintains considerable stability suitable for biomedical applications. Particularly, the differences between the specific TME (lower pH) and the normal physiological environment provide an opportunity to achieve controllable regulation of biomolecules such as proteins, which is mainly caused by the variation of protein surface charge under different pH conditions. At the same time, the reversible nature of electrostatic interactions may lead to disassembly in response to specific stimuli such as acidic TME, which could contribute to controllable drug release. Currently, most of the studies on protein CAT focus only on its oxygen supplementation ability, while investigations of the correlations between CAT surface charge and physiological and pathological microenvironments, which are of great importance for electrostatic assembly and regulation, are rarely reported. On the other hand, fluorescent QDs are capable of multicharge effects due to their ligand-tunable nature, thus allowing them as promising substrates for driving the electrostatic assembly of proteins. Therefore, there is an urgent need to develop TME-responsive protein nanoassemblies based on multicharge electrostatic interactions for effective imaging-guided combined therapy to inhibit tumors.

Herein we designed an intelligent NIR QD-mediated protein nanosystem (Ag_2S@CAT–Ce6@Oxa) based on a multicharged electrostatic self-assembled strategy that can specifically respond to the TME for imaging-guided synergistic PDT/PTT/chemotherapy (**Scheme 1**). Protein CAT was selected as an oxygen-supplemented scaffold with patchy negatively charges distributed on the surface, followed by chemical conjugation with chlorin e6 (Ce6) as a PS via zero-length crosslinking. Then, surface-aminated Ag_2S QDs are introduced as the linking motif with positively charges to trigger the multicharged electrostatic interactions with CAT under physiological conditions, which can not only self-assemble into hierarchical ordered nanostructures, but also effectively load CRC-specific anticancer drug oxaliplatin (Oxa) during the assembled process. Proximity of the acidic TME to the PI of CAT weakened the charge effect that can induce the disassembly of the nanosystem, resulting in the release of the Oxa while maintaining fluorescence imaging, PDT, and PTT capability. Such a smart theranostic nanosystem offers several outstanding features: 1) owing to the greatly relieved tumor hypoxia and the capability of Ce6, enhanced PDT can be realized both in vitro and in vivo; 2) visualization of nanoparticle (NP) accumulation to guide further phototherapy by NIR fluorescence imaging can be highly beneficial for precise and efficient therapy; and 3) encapsulation of anticancer drugs in electrostatic assemblies not only solves the problems of hydrophobicity and targeted delivery. More importantly, by regulating the strength of the charging effect of CAT through the pH characteristics of the TME, the electrostatic assemblies can be effectively controlled to undergo a slow disassembly, which is of great significance in achieving sustained drug release; 4) each candidate in the fabrication of the nanoassemblies possesses intrinsic bioaffinity, enabling them with excellent biocompatibility to be promising for in vivo applications; 5) the synergistic PDT and PTT, together with controlled chemotherapy of the Oxa meditated by the TME can achieve remarkable tumor growth inhibition and prolonged lifespan in mice. Therefore, this work provides a facile way to fabricate a unique type of responsive functional protein-assembled

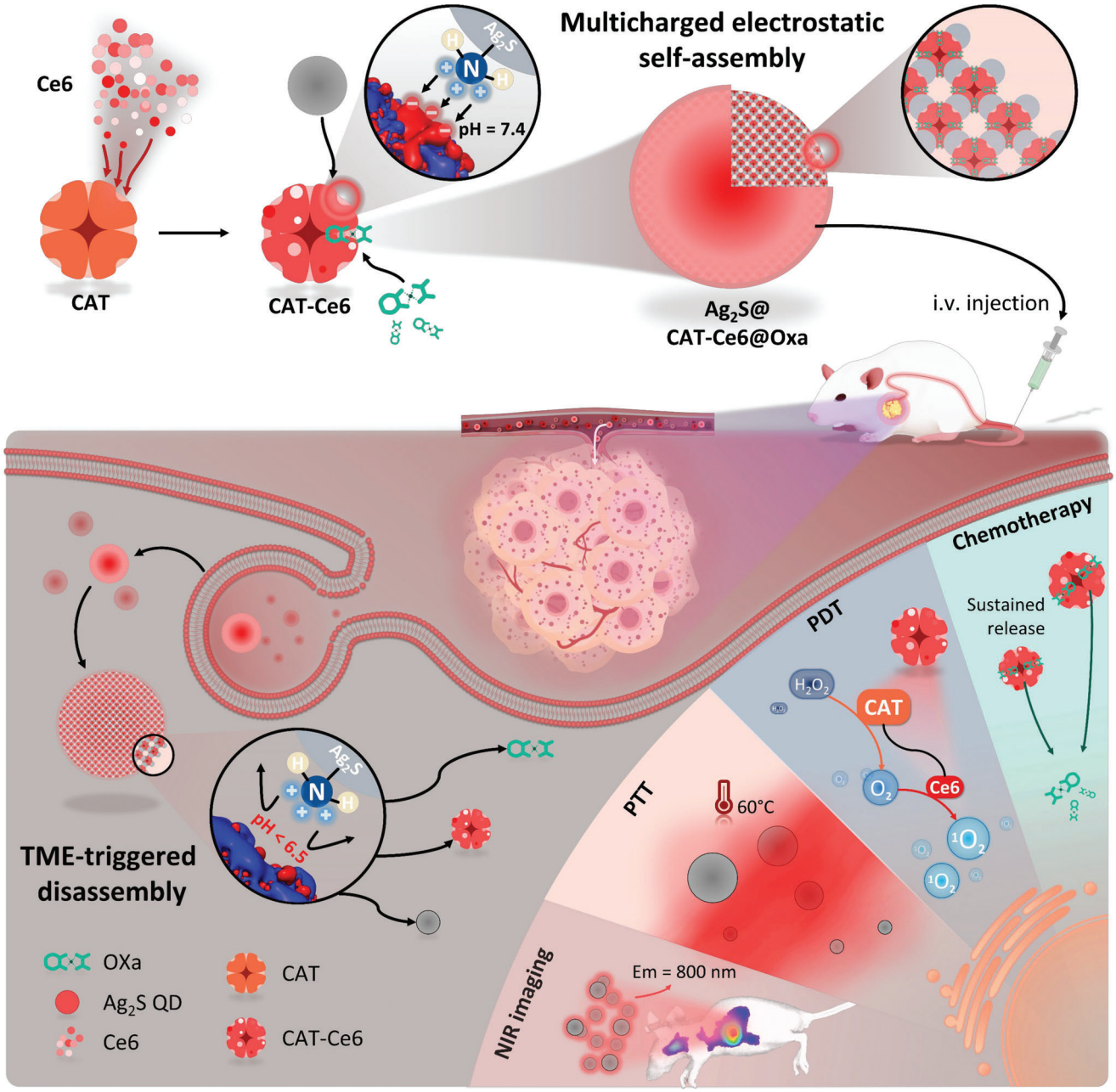

Scheme 1. Schematic illustration of assembly process of Ag_2S@CAT–Ce6@Oxa NPs and NIR imaging-guided PDT/PTT synergistic chemotherapy under the acidic TME via disassembly.

theranostic nanosystem for improved cancer therapy by alleviating tumor hypoxia under the guidance of fluorescence imaging.

2. Results and Discussion

2.1. Construction and Characterization of the Self-Assembled Ag_2S@CAT–Ce6@Oxa

CAT is regarded as a potent enzyme enabled to trigger the breakdown of endogenous H_2O_2 in tumors to generate oxygen. To address the problem of tumor oxygen deprivation, we introduced the natural protein CAT as an important part of the assembly motif, and first used dynamic light scattering (DLS) to measure the size distribution of free CAT. As shown in Figure S2 (Supporting Information), the size of CAT was about 10 nm, which was in well accordance with that in transmission electron microscopy (TEM; Figure S3, Supporting Information). The combination of CAT with PSs can not only solve the water solubility problem of PSs but also improve the efficacy of PDT. In order to achieve this goal, here we covalently modified the conventional PS, Ce6, to CAT via the formation of amide bond. The UV–visible absorbance spectrum of CAT–Ce6 is shown in **Figure 1**a, where

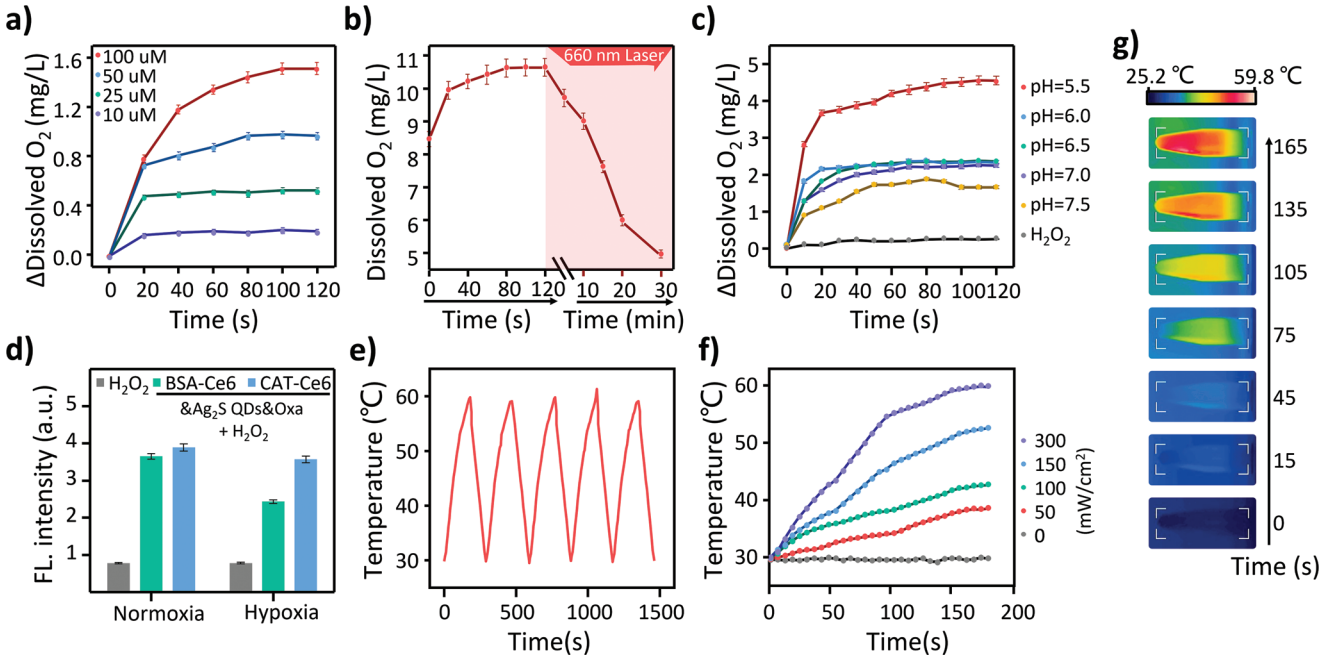

Figure 1. Characterization of Ag_2S@CAT–Ce6@Oxa NPs. a) Normalized absorbance spectrum of free CAT and CAT–Ce6 by UV–vis spectroscopy. b) TEM and HRTEM images (inset) of the Ag_2S QDs. c) The XRD patterns of the Ag_2S QDs (red curve) and the standard Ag_2S QDs (JCPDS card no. 14–0072, black curve). d-i–v) The zeta potential analysis of Ag_2S-3MPA, Ag_2S–NH_2, CAT, CAT–Ce6, and Ag_2S@CAT–Ce6@Oxa NPs, respectively. e,f) DLS analysis and TEM images of the assembled Ag_2S@CAT–Ce6@Oxa NPs at pH = 7.4. g) The average size distribution of the Ag_2S@CAT–Ce6@Oxa NPs at different time points in DMEM, 50 mM PBS, and10% FBS, respectively. h) Molecular docking model of Oxa to CAT.

the covalent modification of CAT–Ce6 led to a redshift of the characteristic peak compared with that of free Ce6 observed at about 660 nm, confirming the successful conjugation of CAT and Ce6. As shown in Figure 1d-iii,iv, the zeta potential of CAT itself was −29.2 mV under simulated physiological conditions (pH = 7.4), while that of CAT–Ce6 after modification was −37.7 mV. Since the covalent modification of CAT–Ce6 consumed a large number of amino groups on the protein surface, CAT–Ce6 showed a strong negative charge under physiological conditions, which not only indicated the successful covalent modification of CAT–Ce6 but also provided a good opportunity for electrostatic assembly.

Another functional-assembled motif Ag_2S QDs were first prepared by a facile one-step synthesis to obtain negatively charged motif.[23] The TEM image (Figure 1b) showed that the prepared Ag_2S QDs were monodispersed with an average size of about 2.59 ± 0.65 nm by measuring the diameter of 303 nanoparticles. Notably, the high-resolution TEM (HRTEM) characterization (Figure 1b, inset) exhibited high crystallinity with clear lattice fringes of d = 0.2604 nm, which could correspond with (−121) crystal facet of Ag_2S. Then, the crystal structure of Ag_2S QDs was further examined by X-ray powder diffraction (XRD). As shown in Figure 1c, the location and relative intensities of the diffraction peaks (red curve) were well agreed with the monoclinic Ag_2S (black line, JCPDS card number 14–0072), indicating the presence of Ag_2S nanocrystals. There appeared two distinct absorption peaks at 1560 and 1414 cm^{-1} in the Fourier transforms infrared (FTIR) spectrum of Ag_2S QDs (Figure S4, Supporting Information), which were attributed to the asymmetric and symmetric stretching vibrations of the carboxylate, confirming the existence of –COOH on the surface of Ag_2S QDs originated from the 3-mercaptopropionic acid (3-MPA) ligands. In order to fabricate a positively rich motif and further enhance the biocompatibility of Ag_2S QDs, six-arm polyethylene glycol amine (6ARM–PEG–NH_2) with multiple positive centers was introduced to be coupled to the surface of Ag_2S QDs via zero-length crosslinking. The obvious change in zeta potential from the initially synthesized Ag_2S QDs of −67.6 mV to the Ag_2S–NH_2 QDs of 64.2 mV had validated the successful preparation of positively charged Ag_2S–NH_2 QDs (Figure 1d-i,ii). After modification, the size of Ag_2S–NH_2 QDs seemed to be increased, and the fluorescence intensity showed a bit stronger compared with the 3-MPA-coordinated Ag_2S QDs (Figures S5 and S6, Supporting Information).

Due to the charge characteristics of the obtained multicomponent motifs, the self-assembly process via multicharged electrostatic interactions was then conducted to construct integrated nanosystems. In order to theoretically verify the feasibility of electrostatic assembly, we first calculated and visualized the electrostatic potential energy results by the Adaptive Poisson–Boltzmann Solver (APBS), adjusting the positive and negative isosurfaces to ±1 kT/e to obtain the electrostatic potential energy isosurface (Figure S1, top, Supporting Information). Further manipulation was conducted to map potential energy on solvent accessible surfaces (Figure S1, down, Supporting Information). The analysis of the isosurface revealed the predominance of negative charges under simulated physiological conditions (pH = 7.4) (Figure S1, Supporting Information). Alongside surface visualization, we also quantified the CAT surface charge and plotted a heat map of the pH and ionic strength dependence of the folded state protein. The most convenient feature extracted from

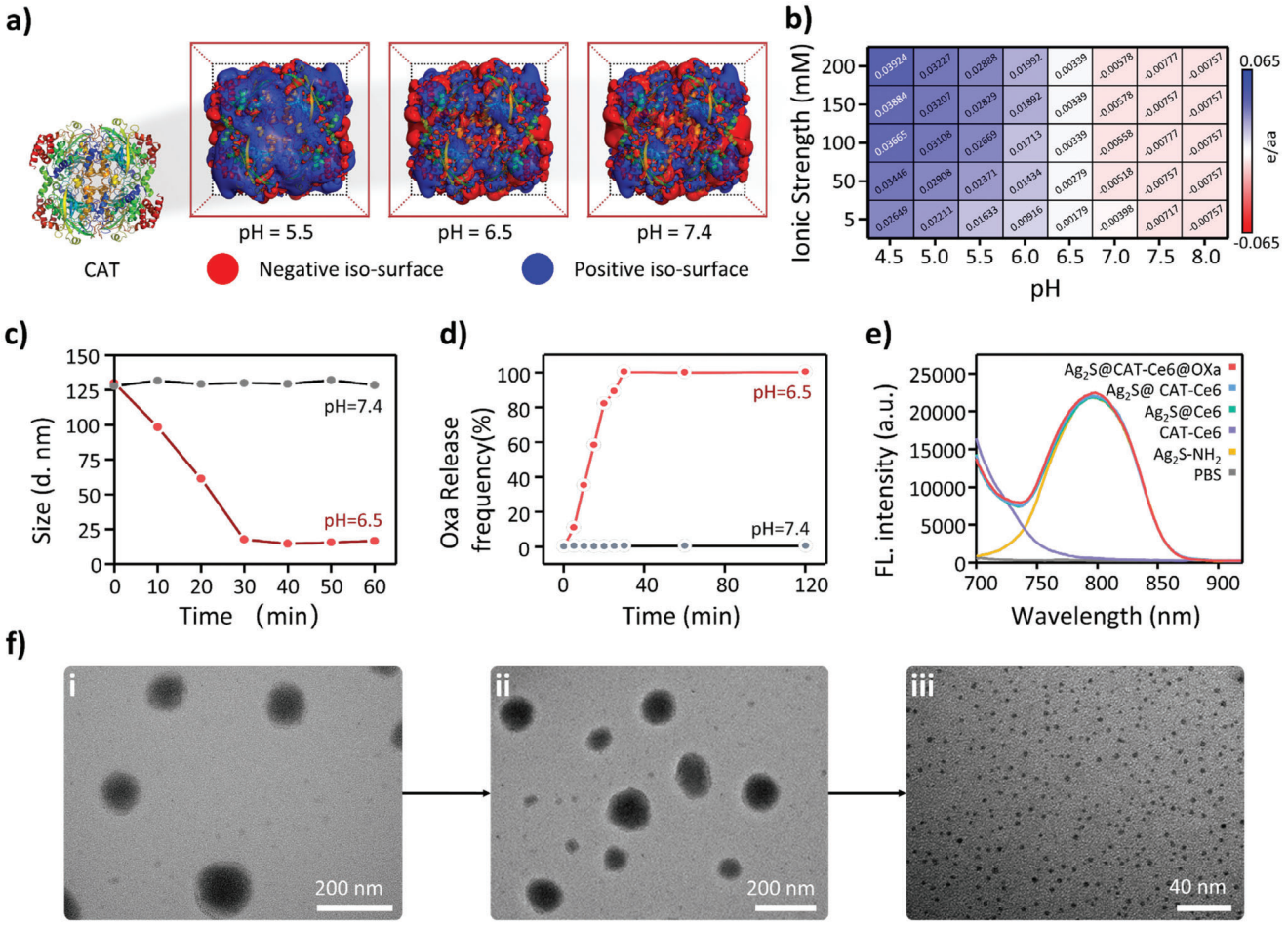

Figure 2. Characterization of the disassembly process. a) Isosurface calculation of protein CAT at pH = 5.5, 6.5, and 7.4. b) Heatmaps showing the various pH and ionic strength dependence. c) The size distribution of the Ag_2S@CAT–Ce6@Oxa NPs at pH = 6.5 in 60 min compared with that at pH = 7.4. d) Oxa release frequency over time in Ag_2S@CAT–Ce6@Oxa NPs at simulated physiological (pH = 7.4) and acidic TME (pH = 6.5) conditions. e) Fluorescence spectra of the assembled and disassembled groups. f) TEM images of the disassembly process of the NPs under PBS buffer solution at pH = 6.5: i–iii) the TEM of the disassembly time points of 0, 10, and 30 min, respectively.

the charge heat map was the predicted sign of net charge, which could confirm that the protein surface electrostatic charge calculated under simulated physiological conditions (pH = 7.4) was indeed negative (**Figure 2**b). These calculations and analysis could provide a strong theoretical basis for the feasibility of protein assembly triggered by electrostatic interactions.

To further optimize the assembly conditions, we modulated the ionic strength to regulate the charge interaction, thus controlling the ordered assembly of CAT and Ag_2S–NH_2 QDs. When no ions were present, they tended to form random aggregates that could be observed in TEM (Figure S7a, Supporting Information). However, too high salt concentration would screen the charge of both candidates that caused the failure of assembly (Figure S7c, Supporting Information). Therefore, we found that appropriate ion strength (50 mM PBS, pH = 7.4) could facilitate the orderly arrangement of the nanoassemblies, which mainly attributed to that only the strong multicharged effect could drive the assembly under such conditions (Figure S7b, Supporting Information). Notably, zeta potential results of the nanoassemblies revealed negligible charge, validating the fact of electrostatic interactions for inducing assembly (Figure 1d-v). Furthermore, DLS results confirmed the formation of monodisperse nanostructures of ≈126 nm upon self-assembly (Figure 1e). TEM characterizations well supported the DLS findings, showing detailed uniform spherical morphology with an average diameter of ≈100 nm (Figure 1f). The larger size shown on DLS was due to the measurement of hydrodynamic diameter. To further investigate the assembly kinetics, we used DLS to record the process of particle size change in the mixed solution at different periods. We found that the particle size of the aqueous solution was increasing with time in 2 h when it finally remained at a stable value (Figure S8, Supporting Information). The kinetic results of the assembled Ag_2S@CAT–Ce6@Oxa NPs strongly supported the formation process of the assemblies.

During the assembly process, anticancer drug Oxa was designed to incorporate into the nanosystem by the conjugation of the hydrophobic region of CAT. As shown in Figure 1h, the molecular docking model gave a powerful explanation of the binding pattern, where Oxa as a ligand could be effectively incorporated via binding to VAL55, SER337, MET339, and ALA345

residues on CAT. Further drug encapsulation experiments could also confirm the effective loading of Oxa in the Ag_2S@CAT–Ce6@Oxa NPs (Figure S9, Supporting Information).

2.2. Stability of the Multicharged Electrostatic Nanoassemblies

Although electrostatic interaction is usually regarded as a long-range weak interaction in supramolecular assembly, multicharge-based electrostatic assembly can overcome the disadvantage that conventional electrostatic assembly is easily perturbed by external conditions and thus has better stability. By analyzing the ionic-strength-dependent charge heat map, it could be found that the calculated electrostatic charge decreased from −0.00717 to −0.00757 as the ionic strength increased from 5 to 50 mM under simulated physiological conditions (pH = 7.4) (Figure 2b). Further increase in ionic strength showed a little effect on the charge change, indicating that the negative charge plateau may be reached at 50 mM. This theory was also consistent with the previous optimization results of assembly conditions (Figure S7b, Supporting Information), highlighting the patch negative charges on CAT surface to enhance the stability of electrostatic interactions.

Furthermore, in order to verify the stability of Ag_2S@CAT–Ce6@Oxa NPs, we dissolved nanoparticles in different buffer solutions (50 mM phosphate buffered saline (PBS), 10% fetal bovine serum (FBS), Dulbecco's modified eagle medium (DMEM)) and measured the size of Ag_2S@CAT–Ce6@Oxa NPs from 0 to 24 h. As shown in Figure 1g, DLS results exhibited that the size of the nanoparticles remained essentially unchanged in the three buffer solutions, showing excellent stability of these self-assembled NPs. Meanwhile, we measured the fluorescence stability of the assembled Ag_2S@CAT–Ce6@Oxa NPs at different times. In comparison with the free Ag_2S–NH_2 QDs, Ag_2S@CAT–Ce6@Oxa NPs could maintain comparable fluorescence signals over a period of time (Figure S10, Supporting Information). These results indicated great potential of the assembled NPs for use in complicated biological environments.

2.3. In Vitro pH-Triggered Disassembly and Sustained Drug Release

To better explore the pH-responsive disassembly process, we selected three representative sets at different pH conditions from the calculated results of the isosurface of CAT and analyzed them in detail. As shown in Figure 2a, the protein isosurface was negatively charged dominant under simulated physiological conditions (pH = 7.4). As the pH decreased to 6.5 or even 5.5, the negative charge of the protein isosurface gradually weakened to ultimately reverse into positively charged. Meantime, this feature was quantitatively analyzed in the heat map, which further confirmed the process of varying the protein electrostatic charge from negative to positive as the pH decreased (Figure 2b). In view of this, we could propose that in the acidic TME, the electrostatic interaction in the assembled system was weakened and insufficient to maintain the electrostatic assembly, and thus a slow disassembly may occur, leading to a sustained release of the drug.

To further study the pH-dependent disassembly behavior of the Ag_2S@CAT–Ce6@Oxa NPs, we simulated an acidic TME (pH = 6.5) and incubated the obtained Ag_2S@CAT–Ce6@Oxa NPs in this environment for 1 h. It was noticed that the Ag_2S@CAT–Ce6@Oxa NPs became smaller and smaller in size with time and finally remained around 15 nm. Under simulated physiological conditions, the assembled Ag_2S@CAT–Ce6@Oxa NPs always remained stable with the size of 125 nm, as shown in Figure 2c. The results of particle size reduction in an aqueous solution indicate that the assembled Ag_2S@CAT–Ce6@Oxa NPs showed a slow disassembly with time at pH = 6.5. To visualize the changes in the disassembly morphology, we performed TEM to observe the disassembly process, and the results are shown in Figure 2f. The initial homogeneous spherical nanoparticles of about 100 nm were gradually disassembled into particles of about 10 nm, which were consistent with the previous DLS results. To further investigate the fluorescence signal changes of the disassembled nanoparticles, we measured the fluorescence spectra of the assembled Ag_2S@CAT–Ce6@Oxa NPs before and after the disassembly, and the results of Figure 2e showed that the fluorescence signal of the nanoparticles remained unchanged, which indicated that the nanoparticles could still maintain a good fluorescence signal even after disassembly.

As the system underwent disassembly, a slow drug release occurred due to the perturbation of the complex biological environment from which the drug Oxa bound to the protein may be dissociated. To further investigate the release process of chemotherapeutic drug Oxa from Ag_2S@CAT–Ce6@Oxa NPs, we measured the UV spectra of the assemblies at different periods. Under normal simulated physiological conditions (pH = 7.4), Ag_2S@CAT–Ce6@Oxa NPs could remain stable without drug leakage for a long period of time. In comparison, the characteristic absorbance peak corresponding to Oxa at 250 nm was slowly increased with time under slightly acidic conditions (pH = 6.5), which indicated that the Oxa was released continuously as the Ag_2S@CAT–Ce6@Oxa NPs disassembled. It can also be observed that the sustained release of Oxa can last for more than 30 min to achieve complete release. All these results suggested that the pH-responsive disassembly of Ag_2S@CAT–Ce6@Oxa NPs in the acidic environment could effectively induce sustained drug release.

2.4. The Catalytic Behavior of Ag_2S@CAT–Ce6@Oxa NPs for the Production of O_2

CAT is a naturally occurring protein that serves as an effective peroxidase to efficiently catalyze the decomposition of H_2O_2 into water and oxygen. Considering that CAT has been partially modified, the catalytic ability of Ag_2S@CAT–Ce6@Oxa NPs needs to be evaluated. Here, enzymatic reaction experiments were carried out in a solution with a certain concentration of H_2O_2 and different pH values, and the O_2 level generated in the enzymatic reaction of Ag_2S@CAT–Ce6@Oxa NPs was measured with a portable oxygen probe. The results revealed that Ag_2S@CAT–Ce6@Oxa nanoparticles were able to maintain their activity of catalytic decomposition of H_2O_2 to O_2 even at lower H_2O_2 levels, and the amount of O_2 produced increased with increasing H_2O_2 concentration (100 μM) (**Figure 3**a), thus could be used for catalytic oxygen production in the TME. In addition, the catalytic efficiency of Ag_2S@CAT–Ce6@Oxa NPs exhibited no significant effect on

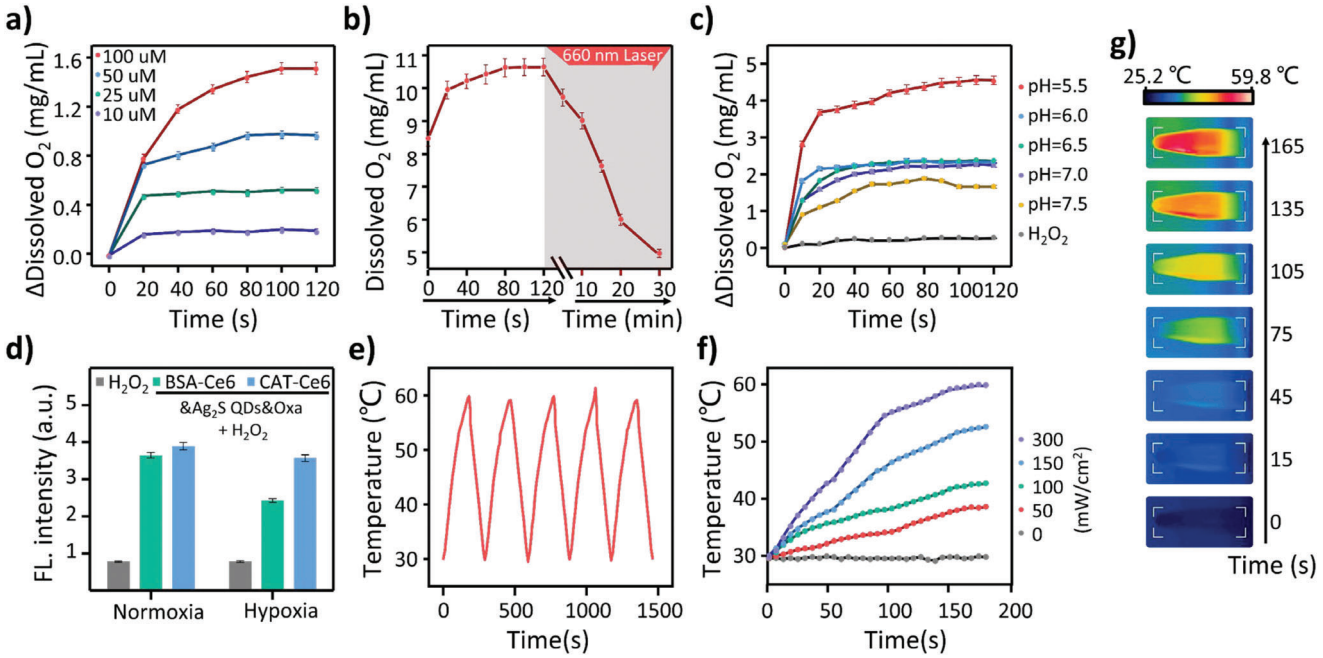

Figure 3. Evaluation of in vitro PDT and PTT performance. a) Oxygen produced by Ag_2S@CAT–Ce6@Oxa NPs in the addition of different concentrations of H_2O_2 solution. b) Dissolved oxygen levels before and after light irradiation. c) Production of oxygen in H_2O_2 (100 μM) solutions of different pH values. d) $^1O_2$ produced by Ag_2S@CAT–Ce6@Oxa NPs or Ag_2S@BSA-Ce6@Oxa NPs in the presence of H_2O_2 under normoxic and hypoxic conditions was measured by fluorescence of SOSG under laser irradiation at 650 nm. e) Photostability of Ag_2S@CAT–Ce6@Oxa NPs under a 600 nm laser irradiation at 300 mW cm^{-2}. f) Photothermal curves of Ag_2S@CAT–Ce6@Oxa NPs at different power densities under 600 nm laser irradiation. g) Photothermal images of different time intervals within 3 min of Ag_2S@CAT–Ce6@Oxa NPs under 600 nm laser irradiation with a laser power of 300 mW cm^{-2}.

the pH in the physiological range (Figure 3c), yet we noticed that the catalytic ability of Ag_2S@CAT–Ce6@Oxa NPs remained robust at pH values below 6.5, indicating that even in acidic TME, Ag_2S@CAT–Ce6@Oxa NPs can still preserve the promising catalytic ability.

To verify the feasibility of Ag_2S@CAT–Ce6@Oxa NPs in PDT, the change in O_2 level was measured at different light intervals under 660 nm irradiation to demonstrate the oxygen consumption during PDT (Figure 3b). The results showed that the oxygen concentration in the Ag_2S@CAT–Ce6@Oxa nanoparticle system decreased significantly with increasing light time, and the oxygen consumption rate was highest at 10–20 min of light. After 15 min of light exposure, a certain level of dissolved oxygen was maintained in the system, thus avoiding the phenomenon of oxygen depletion, while still maintaining a high PDT efficiency. This also provided suitable conditions for PDT in a series of experiments conducted later in cells and in vivo.

2.5. Evaluation of Singlet Oxygen ($^1O_2$) Generation

To verify the feasibility of Ag_2S@CAT–Ce6@Oxa PDT, the ability of nanoparticles to generate singlet oxygen ($^1O_2$) was measured. singlet oxygen sensor green (SOSG) can selectively bind to $^1O_2$, and the oxidation of SOSG will lead to an increase in fluorescence, thus providing a method to monitor the production of $^1O_2$. Under 650 nm laser irradiation with a power density of 300 mW cm^{-2} for 5 min, the fluorescence intensity of different groups with or without assembly of CAT in different environments was measured (Figure 3d). At normal oxygen concentrations, when the Ce6 concentration was consistent, the $^1O_2$ generated from light-triggered Ag_2S@CAT–Ce6@Oxa NPs and Ag_2S@BSA–Ce6@Oxa NPs seemed to be quite pronounced, and both did not show considerable differences. However, under hypoxic conditions, the generation of $^1O_2$ by Ag_2S@BSA-Ce6@Oxa NPs dramatically decreased. For Ag_2S@CAT–Ce6@Oxa NPs, additional oxygen could be provided by CAT catalyzing H_2O_2 in the hypoxic environment, which enabled them to maintain $^1O_2$ production comparable to that in the normoxic environment. As the TME contains a large amount of endogenous H_2O_2 (50–100 μM),[37] Ag_2S@CAT–Ce6@Oxa NPs can effectively alleviate the reduction of PDT efficiency due to hypoxia. This provides hope for achieving better PDT efficacy in hypoxic TME.

2.6. Photothermal Properties of Ag_2S@CAT–Ce6@Oxa

In accordance with previous reports in the literature, certain photothermal conversion properties can be observed in Ag_2S QDs due to their strong absorption in the NIR biological window. In this study, the in vitro photothermal conversion properties of Ag_2S@CAT–Ce6@Oxa were investigated under 600 nm irradiation. The temperature of the solution increased significantly when the power density of the laser was increased from 0 to 300 mW cm^{-2}. At a laser power density of 300 mW cm^{-2}, the temperature of the aqueous Ag_2S@CAT–Ce6@Oxa solution rapidly reached about 60 °C within 3 min (Figure 3f). In addition, we used infrared thermal images to monitor the rapid temperature

rise of Ag_2S@CAT–Ce6@Oxa (200 μg mL^{-1}) under laser irradiation at a laser power of 300 mW cm^{-2} shown in Figure 3g, which showed a remarkable difference compared with PBS solutions (Figure S11, Supporting Information). These results directly demonstrated that Ag_2S@CAT–Ce6@Oxa could efficiently and rapidly convert light energy into heat energy under laser irradiation. To evaluate the photothermal stability of Ag_2S@CAT–Ce6@Oxa, the temperature profiles of the aqueous solution were recorded during five cycles of heating and cooling under laser irradiation (Figure 3e). The results showed no significant temperature attenuation in the solution during each cycle, indicating that Ag_2S@CAT–Ce6@Oxa could be used as a stable light absorber with excellent photothermal effect for PTT in the NIR biological window. These findings provide a promising direction for the development of effective cancer PTT using Ag_2S@CAT–Ce6@Oxa.

2.7. Cellular Uptake and Biocompatibility of Ag_2S@CAT–Ce6@Oxa

To explore the uptake behavior of Ag_2S@CAT–Ce6@Oxa NPs by cells, we measured their intracellular fluorescence intensity due to the NIR imaging capability of the Ag_2S–NH_2 QDs contained in the assembled Ag_2S@CAT–Ce6@Oxa NPs. The nanoassemblies were incubated with HT29 cells for different times (0, 30, 60, and 90 min), and then the cells were imaged by confocal laser scanning microscopy (CLSM). As shown in **Figure 4**a, the fluorescence intensity of Ag_2S@CAT–Ce6@Oxa NPs became stronger as the incubation time increased. The results also showed that the Ag_2S@CAT–Ce6@Oxa NPs exhibited more effective cellular uptake at a 90 min incubation time with the cells (Figure 4d), which indicated that the cells could effectively uptake Ag_2S@CAT–Ce6@Oxa and provided an optimal time window for subsequent PDT treatment at the cellular level.

Moreover, the biocompatibility of nanomaterials is crucial for their application in biological systems, the cytotoxicity of Ag_2S QDs was evaluated using CRC cells (HT29) and the CCK-8 kit. As shown in Figure 4c, the cell survival rate was over 90% even after co-culture of cells with high concentrations of Ag_2S QDs (250 μg mL^{-1}) for 48 h, indicating that the obtained Ag_2S QDs had low cytotoxicity and good biocompatibility, consistent with previous reports. The cytotoxicity of assembled Ag_2S@CAT–Ce6@Oxa on HT29 cells was also investigated, and the results showed that more than 85% of cells survived even though the concentration of Ce6 in its nanoparticles was as high as 16 ppm (Figure 4f), indicating that Ag_2S@CAT–Ce6@Oxa nanoparticles still held low toxicity and satisfactory biocompatibility. Overall, these results suggested that the prepared Ag_2S@CAT–Ce6@Oxa nanoparticles possessed excellent biocompatibility and cellular uptake ability, making them a promising candidate for further development as a theranostic agent.

2.8. Evaluation of Enhanced In Vitro PDT

The intracellular production of single linear oxygen was tested on HT29 cells by pre-incubating them with different nanoparticles for 4 h, including the PBS group, Ag_2S@Ce6, Ag_2S@CAT–Ce6, and Ag_2S@CAT–Ce6@OxaCAT nanoparticles group (equivalent concentration of Ce6: 12 μg mL^{-1}). After co-incubation with cells, laser scanning confocal microscopy imaging was performed using SOSG as a fluorescent $^1O_2$ probe under laser irradiation (300 mW cm^{-2}, 10 min). As shown in Figure 4b, the control group showed almost no fluorescence, while the Ag_2S@Ce6 group without CAT displayed a lighter green fluorescence compared to the control group. Excitingly, both Ag_2S@CAT–Ce6 and Ag_2S@CAT–Ce6@Oxa groups showed bright green fluorescence. Additionally, the cellular fluorescence intensity of the four groups was quantified (Figure 4e), and the results demonstrated that treatment with Ag_2S@CAT–Ce6 and Ag_2S@CAT–Ce6@Oxa NPs enhanced the generation of $^1O_2$. The maintenance of comparable $^1O_2$ production in these two groups was attributed to the improved PDT efficiency by the existence of CAT, which alleviated the hypoxic condition.

To further verify the enhanced PDT efficiency of Ag_2S@CAT–Ce6@Oxa, cell viability of HT29 was investigated. The phototoxicity of different groups containing a range of Ce6 concentrations was determined using the standard 3-(4,5-dimethylthiazol-2-yl)-2,5-diphenyltetrazolium bromide (MTT) method when irradiated with a 650 nm NIR laser. As shown in Figure 4g, both the Ag_2S@CAT–Ce6 and Ag_2S@CAT–Ce6@Oxa groups exhibited comparable phototoxicity to HT29 cells, higher than that of the Ag_2S@Ce6 group. The results showed that the Ag_2S@CAT–Ce6@Oxa had enhanced generation of $^1O_2$ compared to the control groups and had the potential to enhance PDT efficiency in cancer therapy.

2.9. Assessment of the Therapeutic Efficacy under Normoxic and Hypoxic Conditions

Hypoxia diminishes the production of singlet oxygen, a key component of the PDT process, leading to a decrease in the effectiveness of PDT in treating tumors. In addition, hypoxia stimulates the production of HIF-1α, a transcription factor that promotes cell survival under hypoxic conditions and leads to tumor resistance to PDT. Therefore, overcoming hypoxia barrier is critical to the success of PDT in cancer therapy. To evaluate the therapeutic efficacy under normoxic and hypoxic conditions, the HT29 cells co-incubated with Ag_2S@CAT–Ce6@Oxa were treated with Calcein-AM/PI to study live/dead cell situations (**Figure 5**a). The effect of killing tumor cells in vitro showed that under normal oxygen conditions, compared with the PBS group, Ag_2S@Ce6, Ag_2S@CAT–Ce6, and Ag_2S@CAT–Ce6@Oxa had a certain degree of red and green fluorescence (red stands for living cells and green stands for dead cells), revealing moderate therapeutic effects. We noted that even under hypoxia conditions, Ag_2S@CAT–Ce6@Oxa NPs could still maintain comparable cell-killing ability to normoxic conditions, which was further analyzed quantitatively to obtain more intuitive results (Figure 5b). This indicated that with the help of the self-assembly system, the intracellular Ag_2S@CAT–Ce6@Oxa NPs were able to provide oxygen to the hypoxic conditions, thus enhancing the killing effect of specific laser-triggered PDT on CRC cells.

Apoptosis detection of HT29 cells in different treatment groups can also be well quantitatively studied. Under laser irradiation, all the groups resulted in a certain number of apoptotic cells except for the control group. Notably, the Ag_2S@CAT–

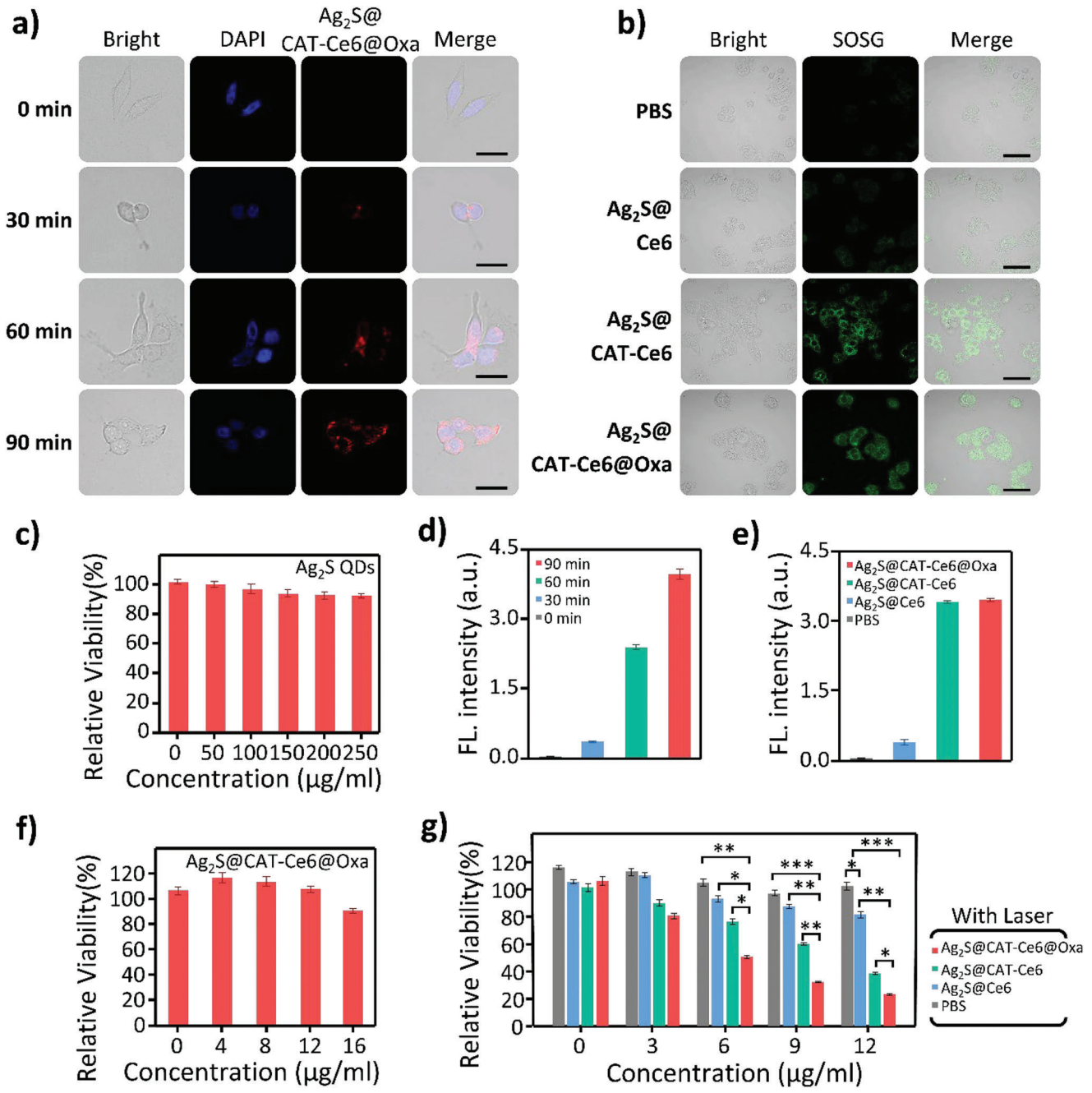

Figure 4. In vitro cellular internalization and cytotoxicity of Ag_2S@CAT–Ce6@Oxa NPs. a) Laser confocal fluorescence micrographs of HT29 cells after incubation with Ag_2S@CAT–Ce6@Oxa NPs at different times. The scale bar is 25 μm. b) Different nanoparticles incubated with HT29 cells followed by internal $^1O_2$ detection using SOSG as a probe. Scale bars: 50 μm. c) In vitro relative viabilities of HT29 cells treated with Ag_2S QDs. d) Corresponding fluorescence quatification of (a). e) Corresponding quantitative fluorescence analysis of (b). f) Ag_2S@CAT–Ce6@Oxa NPs after 24 h treatment. Error estimates are calculated based on triplicate samples. g) Cell viability assay of Ag_2S@Ce6, Ag_2S@CAT–Ce6, and Ag_2S@CAT–Ce6@Oxa NP-treated HT29 cells in hypoxic conditions under 650 nm light irradiation (concentration of Ce6:12 μg mL^{-1}; 650 nm laser power density: 300 mW cm^{-2}; irradiation time: 5 min; $n = 3$, $^*p < 0.05$, $^{**}p < 0.01$, and $^{***}p < 0.001$).

Ce6@Oxa group caused about 60.79% of cell apoptosis, indicating that the phototherapy effect of NIR-induced Ag_2S@CAT–Ce6@Oxa led to cell death mainly through apoptosis rather than necrosis (Figure 5e). Then, we were interested in obtaining an understanding of how the levels of HIF-1α in cancer cells in a hypoxic environment change after incubation with different treating groups. The expression level of HIF-1α in tumors was caused by hypoxia, which can be analyzed by western blot as an indicator of hypoxia. As the results showed, the expression level of HIF-1α was significantly higher in the Ag_2S@Ce6 group compared to the control group, and the expression level of HIF-1α was significantly decreased in the Ag_2S@CAT–Ce6 and

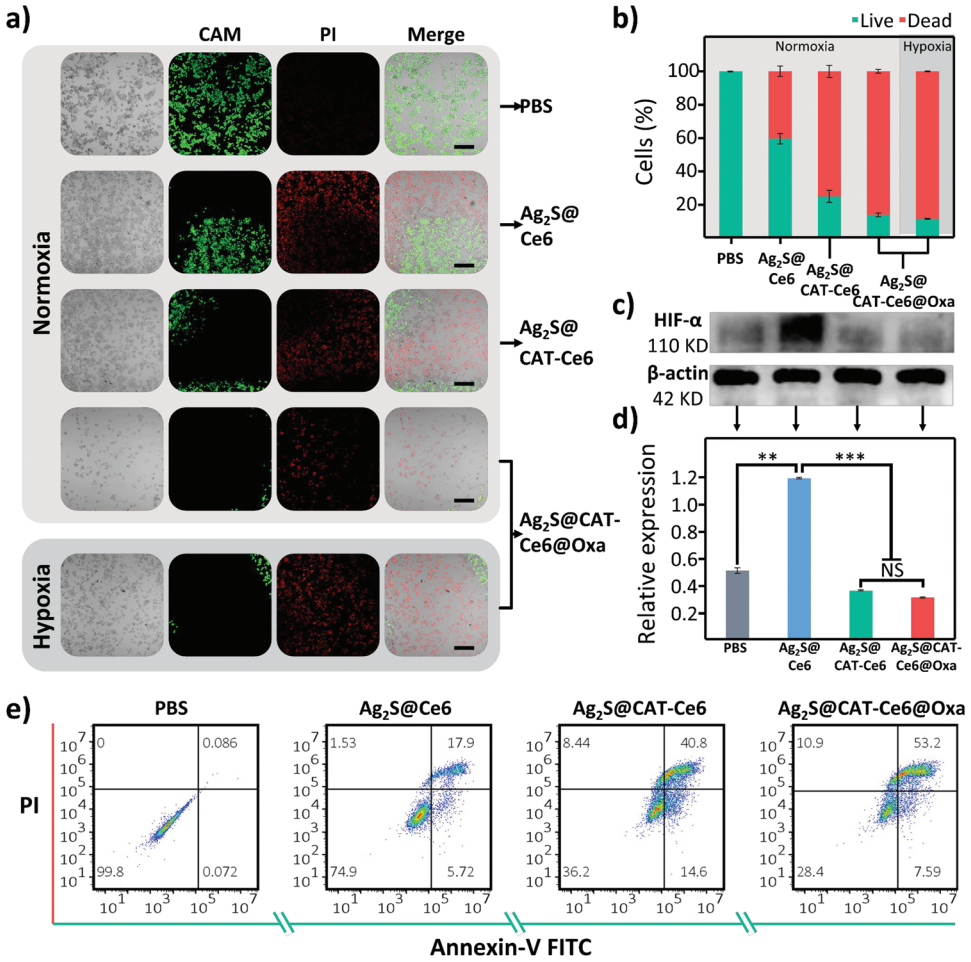

Figure 5. Evaluation of Ag_2S@CAT–Ce6@Oxa NPs for in vitro synergistic treatment of HT29 tumor cells. a) The live/dead staining of HT29 cells and b) corresponding fluorescence quantitative analysis histogram treated with PBS, Ag_2S@Ce6, Ag_2S@CAT–Ce6, and Ag_2S@CAT–Ce6@Oxa NPs by 650 nm laser illumination under normoxic and hypoxic conditions. The green signal of Calcein-AM represents live cells and the red signal of propidium iodide (PI) represents dead cells (concentration of Ce6: 12 μg mL^{-1}). The scale bar is 200 μm. c,d) Western blot analyses of HIF-1α protein expression in HT29 cells treated with PBS, Ag_2S@Ce6, Ag_2S@CAT–Ce6, and Ag_2S@CAT–Ce6@Oxa NPs under hypoxic conditions. Western blot analysis was performed three times. The data are presented as the mean ± standard error of the mean ($n = 3$), where n indicates the number of independent samples. The statistical analysis was performed using a one-way analysis of variance (ANOVA). NS: no statistical significance, $^*p < 0.05$, $^{**}p < 0.01$, and $^{***}p < 0.001$. e) Annexin V-FITC/PI staining followed by flow cytometry analysis was performed to evaluate the cell death mechanism under hypoxic conditions after treatment with PBS, Ag_2S@Ce6, Ag_2S@CAT–Ce6, and Ag_2S@CAT–Ce6@Oxa NPs in the presence of 650 nm laser irradiation.

Ag_2S@CAT–Ce6@Oxa groups relative to Ag_2S@Ce6. In addition, there was almost no difference in the HIF-1α expression levels of Ag_2S@CAT–Ce6 and Ag_2S@CAT–Ce6@Oxa. The evidence confirmed that well-engineered Ag_2S@CAT–Ce6@Oxa nanoprobes can effectively relieve hypoxia and improve the efficacy of PDT, thus achieving a good killing effect on tumor cells (Figure 5c,d).

2.10. In Vivo NIR Imaging-Guided Synergistic PDT/PTT/Chemotherapy

Motivated by the impressive photothermal conversion ability of Ag_2S@CAT–Ce6@Oxa NPs observed in vitro, we investigated their performance for PTT in vivo after intravenous administration. First, we established a subcutaneous xenograft tumor model in nude mice and divided the BALB/c HT29 tumor-bearing nude mice into two groups: control and Ag_2S@CAT–Ce6@Oxa. After the nanoparticles were injected for 12 h, the mice were exposed to NIR laser for 3 min, and the real-time temperature of the tumor area was monitored using infrared thermography (**Figure 6**b). The results showed that the temperature at the tumor site of mice injected with Ag_2S@CAT–Ce6@Oxa rapidly increased by 29.6 °C during the first 3 min and then maintained at 59.5 °C. In contrast, the tumor temperature of the PBS group exhibited only slight fluctuations, and the final temperature was maintained at 31.4 °C, which was almost identical to the initial tumor site temperature. These findings indicate that Ag_2S@CAT–Ce6@Oxa nanoparticles are highly effective at elevating the local tumor temperature under NIR irradiation and have superior in vivo photothermal ability.

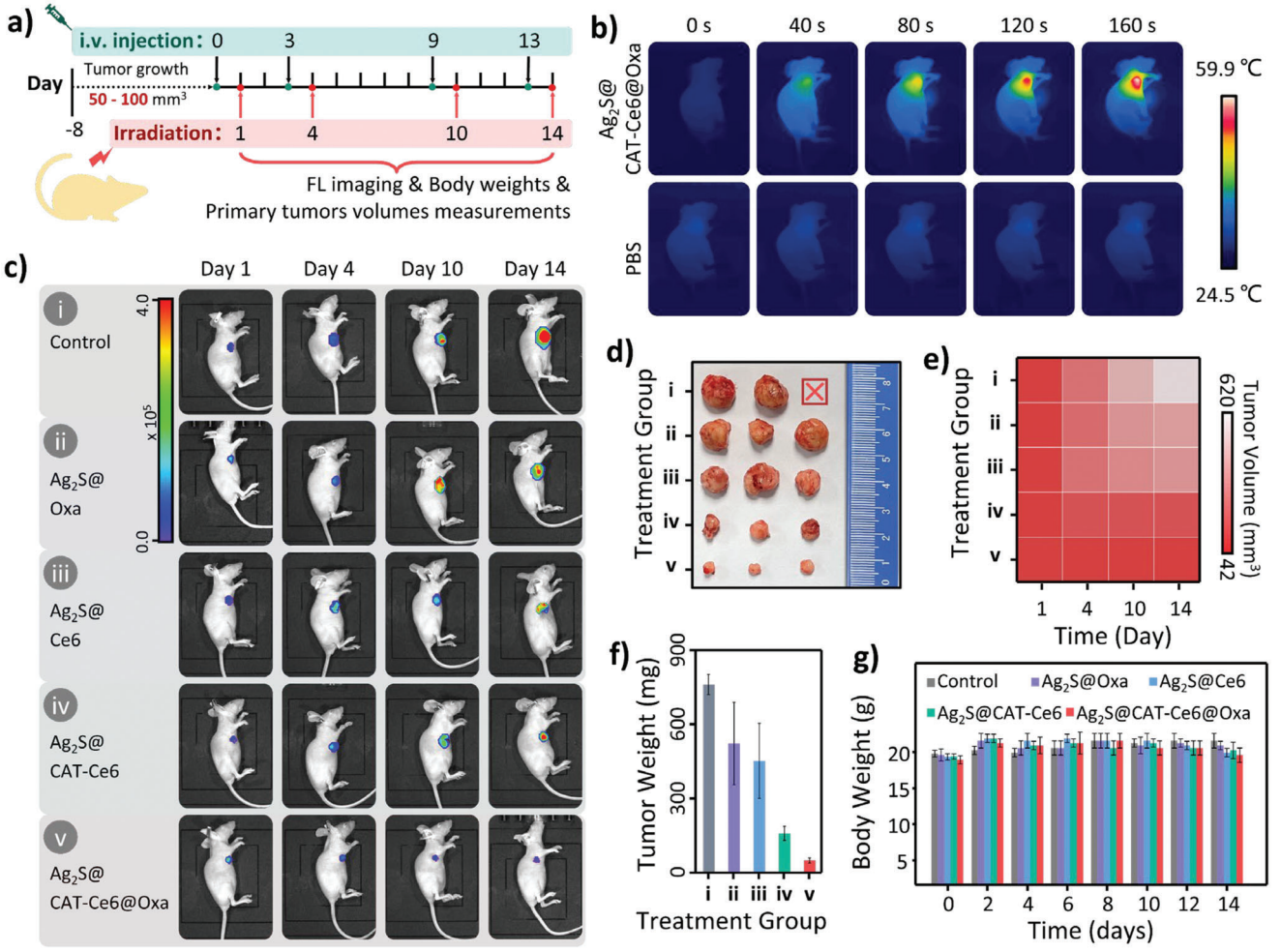

Figure 6. In vivo NIR imaging-guided synergistic therapy. a) Schematic diagram of the BALB/c nude xenograft colon cancer model construction and in vivo NIR light-triggered combination therapy-mediated antitumor treatment plan in mice. b) Infrared thermography of HT29 tumor-bearing mice was injected with PBS (pH value 7.4, 50 mM) and Ag_2S@CAT–Ce6@Oxa NPs (2 mg mL^{-1}, 200 µL). c) In vivo fluorescence images of HT29 tumor-bearing nude mice postsynergistic therapy with intravenously instilled control, Ag_2S@Oxa, Ag_2S@Ce6, Ag_2S@CAT–Ce6, Ag_2S@CAT–Ce6@Oxa NPs. d) Photographs of all groups of colorectal tumors collected at the end of treatment on day 14. e) Tumor growth volumes of HT29 tumor-bearing mice after treatment in various groups ($n = 3$ bio-independent samples). f) Weight of colorectal tumors collected from and g) body weight variations of nude mice on day 14 after the first therapy.

To investigate the effect of synergistic treatment with Ag_2S@CAT–Ce6@Oxa nanoparticles in vivo, BALB/c HT29 tumor-bearing nude mouse model was also utilized. On the eighth day after subcutaneous injection of HT29 cell clusters into nude mice, subcutaneous colorectal tumors grew to 50–100 mm^3, allowing for in vivo synergistic treatment experiments guided by NIR imaging (Figure 6a). The constructed BALB/c HT29 tumor-bearing nude mice were divided into five treatment groups, which included Ag_2S QDs as control, Ag_2S@Oxa NPs, Ag_2S@Ce6 NPs, Ag_2S@CAT–Ce6 NPs, and Ag_2S@CAT–Ce6@Oxa NPs (doses: Ce6 = 3.0 mg kg^{-1}, Oxa = 5 mg kg^{-1}). Each group was monitored over 14 days to evaluate the therapeutic effect of the nanoparticles in vivo at different time points with the help of a small animal imaging apparatus, which was performed as tail vein injection the night before imaging. To investigate the enrichment time of Ag_2S@CAT–Ce6@Oxa nanoparticles reaching the tumor site in nude mice, in vivo fluorescence imaging was performed to monitor the fluorescence signal at the tumor site after tail vein injection of nanoparticles. The fluorescent signals at the tumor site were monitored over time, and the maximum intensity was observed 12 h after the injection of nanoparticles into the bloodstream. However, the fluorescent signal then decreased to half its maximum intensity at the 24th hour. The mice treated immediately with Ag_2S@CAT–Ce6@Oxa nanoparticles were sacrificed for ex vivo imaging of their major organs (Figure S13, Supporting Information). The results showed fluorescent signals in both the tumor and liver, while other major organs such as the spleen, kidney, heart, and lung exhibited minimal fluorescent signals. The fluorescence signal of the tumor site in mice was then quantified at different time intervals, and it was found that the fluorescence signal reached its highest at 12 h after injection, which was in accordance with the previous results. The optimal light time point for the next step of performing laser treatment time was determined accordingly.

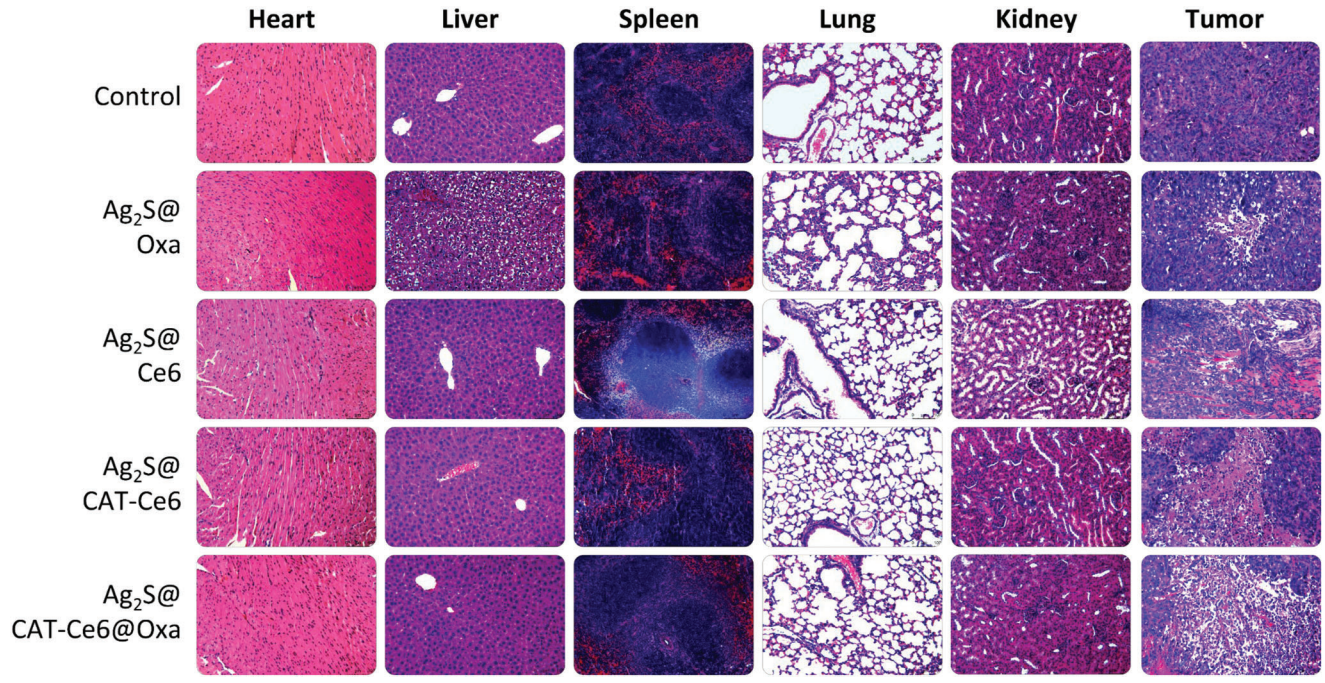

Figure 7. H&E-stained slices of the main organs including heart, liver, spleen, lung, kidney, and tumor from different groups of mice.

The tumor sites of the nude mice were irradiated for 10 min with a 660 nm laser at 300 mW cm^{-2}. In vivo fluorescence imaging was performed with the IVIS Spectrum small animal in vivo optical imaging system to record tumor progression in tumor-bearing mice on days 1, 4, 10, and 14 after illumination (Figure 6c). The relative tumor growth volume is shown in Figure 6e. It was observed that the Ag_2S@CAT–Ce6@Oxa nanoparticle treatment group exhibited the highest tumor-resistance efficacy among all the groups, indicating that it had the greatest inhibitory effect on tumor growth. The Ag_2S@Oxa, Ag_2S@Ce6, and Ag_2S@CAT–Ce6 groups presented certain degree of tumor inhibition compared to the control group. The tumors were excised and weighed in all treatment groups after 14 days (Figure 6d,f). The results indicated that the tumor masses of the Ag_2S@CAT–Ce6 and Ag_2S@CAT–Ce6@Oxa groups were significantly smaller than that of the other groups, especially the Ag_2S@CAT–Ce6@Oxa group. Both the fluorescence images and the photographs of the tumors in live mice (Figure S14, Supporting Information) suggested that the tumors in this group were the smallest and had the lowest mass among all the tumors. The Ag_2S@Oxa NPs and Ag_2S@Ce6 NPs displayed some suppressive effect on tumor growth compared to the control group, possibly because their Ag_2S QDs contain chemotherapeutic drugs or PSs that aroused some therapeutic effect. The pictures of the tumor exfoliation and the quantification of the tumor mass after treatment with the assembled Ag_2S@CAT–Ce6@Oxa nanoparticles containing both chemotherapeutic agents and PSs revealed that the PDT/PTT synergistic chemotherapy treatment with Ag_2S@CAT–Ce6@Oxa nanoparticles in vivo was the most effective in achieving efficient antitumor therapy. Relative tumor growth inhibition values also revealed the satisfactory anticancer therapy (Figure S15, Supporting Information). Based on the above results, Ag_2S@CAT–Ce6@Oxa NPs showed superior PDT/PTT/chemotherapy synergistic therapeutic efficacy to effectively inhibit tumor growth.

2.11. In Vivo Biosafety

None of the treated mice exhibited major systemic toxicity, as their weight was maintained at healthy levels (Figure 6g). To evaluate the systemic toxicity of the five treatment groups during the treatment of tumor-bearing mice, major organs, such as the heart, liver, spleen, lungs, kidneys, and tumors, were collected for histological examination in each group. As demonstrated in **Figure 7**, no significant organ damage was observed in the histological tests, except for some hepatocyte disorganization and interstitial thickening in the lungs of the Ag_2S@Oxa group in Hematoxylin and Eosin (H&E) staining. The existence of certain liver and lung damage in Ag_2S@Oxa may be due to the toxicity of free chemotherapeutic drugs to mice, while the slow release of chemotherapeutic drugs in Ag_2S@CAT–Ce6@Oxa within the acidic TME can better exert the anticancer effect of PDT/PTT synergistic chemotherapy and maintain good biosafety. In conclusion, all these results demonstrated that Ag_2S@CAT–Ce6@Oxa NPs held promise as a nanomedicine for NIR-based imaging-guided PDT/PTT synergistic chemotherapy to treat CRC with improved safety and therapeutic efficacy compared to the clinical use of tail vein injection-dependent Oxa.

3. Conclusion

In conclusion, we have successfully designed an intelligent NIR QDs-mediated protein nanosystem (Ag_2S@CAT–Ce6@Oxa) based on a multicharged electrostatic self-assembled strategy for

imaging-guided synergistic PDT/PTT/chemotherapy in colorectal cancer. The unique design of the nanosystem relies on the surface charge of the oxygen-supplemented protein CAT, which is regulated by the pH characteristics of the TME, enabling controllable disassembly and release of the anticancer drug Oxa. The multicharge electrostatic interactions between CAT and aminated Ag_2S QDs and the covalent conjugation of Ce6 as a PS via zero-length crosslinking allow for the formation of hierarchical ordered nanostructures, which can effectively load and deliver Oxa to the tumor site. The nanosystem shows remarkable therapeutic efficacy in vitro and in vivo, achieving enhanced PDT and PTT as well as controlled chemotherapy. Additionally, NIR fluorescence imaging enabled precise visualization and guidance of the nanoparticle accumulation for further therapy. This work highlights the potential of the multicharge electrostatic self-assembly strategy as a facile and effective way to fabricate TME-responsive functional protein-assembled theranostic nanosystems for efficient and safe cancer therapy, and provides a potential solution to the current challenges in the field of cancer therapy.

4. Experimental Section

Materials: Silver nitrate (≥99.0%), 3-MPA (liquid, ≥99.0%), CAT (bovine origin), and dihydroporphyrin (light protected and dried, ≥95%) were purchased from Sigma–Aldrich (St Louis, MO, USA), while 6ARM–PEG–NH_2 (M_W = 10 000) was obtained from Ponsure (Shanghai, China). Rabbit anti-HIF-1α monoclonal antibody (ab179483) and Anti-beta Actin antibody (ab8226) were both purchased from Abcam (Shanghai, China). The ultrapure water (18 MΩ cm^{-1}) utilized in the experiment was produced by Milli-Q Water Perfusion System (Billerica, MA, USA). All additional reagents were obtained from one commercial source and were of an analytical reagent type used with no further purification.

Instruments: The fluorescence spectra were measured using an FL-QM spectrophotometer (Horiba, Japan). DLS) data were analyzed by an SZ-100Z2 size analyzer (Horiba, Japan). XRD patterns were measured by a D8 Advance X-ray diffractometer (Bruker, Germany). TEM images were acquired by HT7800 (Hitachi, Japan) machine at an accelerated voltage of 120 kV. FTIR spectra were measured by a Thermo-Scientific Nicolet iS50 FTIR spectrometer. Oxygen content was determined by a Mettler Multi InLabOptiOx dissolved oxygen meter. Temperature changes were recorded by a handheld portable infrared thermography (FLIR, USA). Small animal in vivo fluorescence imaging was obtained by an IVIS Lumina series XR system (PerkinElmer, USA).

Preparation of Ag_2S@CAT–Ce6@Oxa NPs: Ag_2S@CAT–Ce6@Oxa NPs were prepared by a self-assembly strategy. Ag_2S QDs solution and CAT–Ce6 solution were mixed by ultrasound for 0.5 h at different weight ratios (1:7.5–7.5:1). Then, Oxa (0.5 mg, 100 µL) was predissolved with a mixture of methanol and dimethyl sulfoxide (DMSO), then added dropwise to the buffer solution (pH = 7.4, 50 mM) and stirred in a dark environment at room temperature for 2 h, and then the purified Ag_2S@CAT–Ce6@Oxa NPs were further centrifuged for 10 min at a rotation speed of 14 000 rpm to remove the free CAT–Ce6, Ag_2S QDs, and Oxa, and finally to obtain Ag_2S@CAT–Ce6@Oxa NPs. When the weight ratio of Ag_2S QDs solution to CAT–Ce6 solution was 1:7.5 and the Oxa content was 0.5 mg mL^{-1}, the Oxa loading frequency was detected to be 10 ± 0.3% calculated from the UV spectrum. The same method was also used to obtain Ag_2S@Oxa NPs and Ag_2S@BSA-Ce6@Oxa NPs. The morphology of the following samples, free CAT, Ag_2S quantum dots, and assembled/disassembled Ag_2S@CAT–Ce6@Oxa nanoparticles, was characterized using TEM. The zeta potential and nanoparticle size of the samples were measured using DLS. The crystal structure of the Ag_2S quantum dots was characterized using XRD. Additionally, the UV absorption spectra were measured by a UN-600 UV–Vis NIR spectrophotometer and fluorescence spectra of the various samples were measured using an FL-QM spectrophotometer.

Release Behavior upon pH-Responsive Disassembly: DLS could be used to measure the hydrodynamic size distribution of particles in solution. The obtained solutions of Ag_2S@CAT–Ce6@Oxa NPs were adjusted to about pH = 6.5, and the size of their nanoparticle distribution in solution at different times (0, 10, 20, 30, 40, 50, and 60 min) was first monitored by DLS. Furthermore, TEM was used to observe the visual changes of the nanostructures during the disassembly process, which could provide detailed information on the size, shape, and aggregation state of the particles. The disassembled nanoparticle solutions at different times were subjected to TEM sampling and then their nanoparticle morphology distribution was observed by TEM.

Generation of $^1O_2$ by Ag_2S@CAT–Ce6@Oxa NPs: To evaluate the ability of Ag_2S@CAT–Ce6@Oxa NPs to produce $^1O_2$ under normoxic and hypoxic conditions, the experimental procedure was as follows: BSA-Ce6@Ag_2S QDs@Oxa NPs and CAT–Ce6@Ag_2S QDs@Oxa NPs (Ce6: 12 µg mL^{-1}) were incubated with SOSG (3 µg) dissolved in methanol in a buffered solution containing the same concentration of H_2O_2. The samples were subjected to laser irradiation (650 nm, 300 mW cm^{-2}) under both conditions of nitrogen purging and no purging. The single-linear state of oxygen produced by the samples under different conditions was measured. The H_2O_2 (100 µM) in the experiment was chosen to simulate the H_2O_2 concentration in the oxygen-depleted TME. The ability of the generated $^1O_2$ was determined by evaluating the fluorescence signal of SOSG at 528 nm under 494 nm excitation.

Cellular Uptake Capacity of CAT–Ce6@Ag_2S QDs@Oxa NPs: HT29 cells was cultured overnight and then adding Ag_2S@CAT–Ce6@Oxa NPs (Ce6: 12 µg mL^{-1}) to a fresh medium. After incubation for 0, 30, 60, and 90 min, the cells with aseptic PBS were washed three times. Then, 4,6–diamino–2–phenylindole (DAPI, 200 µL) was added to each culture dish for staining and treated for 10 min before re-washing with aseptic PBS three times. Finally, the uptake behavior of nanoparticles by the cells was observed using CLSM.

Intracellular Antitumor Properties: HT29 cells were grown in confocal dishes and incubated for 24 h to achieve proper cell density. Then, different nanoparticles (PBS, Ag_2S@Ce6, Ag_2S@CAT–Ce6, and Ag_2S@CAT–Ce6@Oxa NPs with a Ce6 concentration of 12 µg mL^{-1}) were added and incubated with the cells for 4 h to allow sufficient contact between the nanoparticles and the cells. After incubation, the cells were exposed to laser irradiation (650 nm, 300 mW cm^{-2} for 3 min) to excite the PS within the nanoparticles to produce $^1O_2$. Then, 10 µM of SOSG probe was added to be reacted with $^1O_2$ for 10 min. Finally, the cells were washed three times with PBS and imaged by CLSM to observe the change in the fluorescence intensity of SOSG to determine the production and distribution of $^1O_2$.

To visualize the viability of HT29 cells, they were subjected to various treatments, including PBS, Ag_2S@Ce6, Ag_2S@CAT–Ce6, and Ag_2S@CAT–Ce6@Oxa NPs, with a Ce6 concentration of 12 µg mL^{-1}. The treatments were applied for 12 h, followed by a laser irradiation at 650 nm of 300 mW cm^{-2} for 3 min. After 4 h of incubation, the cells were stained with Calcein-AM/PI for 30 min. The labeled cells were then washed three times with PBS and imaged by CLSM using excitation wavelengths of 488 and 561 nm for Calcein-AM and PI, respectively.

In Vivo Fluorescence Imaging: In the experiment, when the tumor volume of HT29 tumor-bearing mice reached about 60 mm^3, the mice were randomly divided into five groups with each group of three mice. They were then intravenously injected with different candidates through the tail vein, including the control group (Ag_2S: 1 mg kg^{-1}), Ag_2S@Oxa, Ag_2S@Ce6, Ag_2S@CAT–Ce6, and Ag_2S@CAT–Ce6@Oxa NPs (with the main component content of Oxa: 5 mg kg^{-1}, Ce6: 1 mg kg^{-1}, and 200 µL). After 12 h of injection, the mice were anesthetized (using pentobarbital, at a concentration of 6 mg mL^{-1} with a dose of 10 µL g^{-1}), and then conducted tumor fluorescence imaging using the IVIS Lumina series XR system. During this process, the laser wavelength was set to 600 nm, and the emission and collection wavelengths were set to 800 nm to evaluate the accumulation time of the nanoparticles in the tumor and assess the synergistic therapeutic effect.

In Vivo Tumor Inhibition: All groups were intravenously injected with Ag_2S QDs as control, Ag_2S@Oxa, Ag_2S@Ce6, Ag_2S@CATCe6, Ag_2S@CAT–Ce6@Oxa NPs (Ag_2S: 1 mg kg^{-1}, Oxa: 5 mg kg^{-1}, Ce6: 1 mg kg^{-1}, and 200 µL) on days 0, 3, 9, and 10. Body weight and tumor volume of all nude mice were documented at regular intervals throughout the treatment period. They were also recorded every 4–5 days. Tumor volume was calculated by the following equation: $V = \text{length} \times \text{width} \times \text{height} \times \pi/6$. The subcutaneous tumor growth inhibition (TGI) value was calculated by the following formula: $TGI = (1 - B/A) \times 100\%$ (A is the mean tumor weight in the control group, B is the mean tumor weight in the treatment group). The animal experiments should be terminated when the nude mice reached a weight loss of 20–25% or when the tumors were more than 20 mm in diameter in any dimension.

Animal Ethics Statement: BALB/c nude mice (3–4 weeks old, male) were performed in accordance with the guidelines for Care and Use of Laboratory Animals of Hainan Medical University, and approved by the Animal Ethics Committee of Hainan Medical University. (Approval number: HYLL-2022-026).

Statistical Analysis: All experiments were conducted three times which performed using GraphPad Prism software version 8.0 (GraphPad Prism Software), Excel 2016 software (Microsoft), and Origin2021, and the statistical analysis presented the mean ± standard deviation (SD). The statistical analysis was performed using a one-way analysis of variance (ANOVA). Multiple comparisons between groups were performed using analysis of two-way analysis of variance, and statistical significance was defined as $^*p < 0.05$, $^{**}p < 0.01$, and $^{***}p < 0.001$.

Supporting Information

Supporting Information is available from the Wiley Online Library or from the author.

Acknowledgements

M.J.H. and Z.Y.C. contributed equally to this work. This work was supported by the National Natural Science Foundation of China (Grant Nos. 22164009, 22264013, 22064009, 82202647, and 21961010), Hainan Province Science and Technology Special Fund (Grant Nos. ZDYF2022SHFZ311, ZDYF2021SHFZ244, ZDYF2021SHFZ245, ZDYF2021SHFZ219, and ZDYF2022SHFZ080), Hainan Provincial Natural Science Foundation of China (Grant Nos. 820RC655 and 322QN309), Natural Science Research Talent Project of Hainan Medical University (Grant No. JBGS202101), Hainan Province Clinical Medical Center (2021), Innovative Research Subjects for Postgraduates of Hainan Province General Higher Education Institutions (Hys2020-363, Hyb2020-58, and Hys2020-375), and Hainan Medical University Master Class B Project (Project No. HYYS2021B03).

Conflict of Interest

The authors declare no conflict of interest.

Data Availability Statement

The data that support the findings of this study are available on request from the corresponding author. The data are not publicly available due to privacy or ethical restrictions.

Keywords

controlled drug release, electrostatic interactions, fluorescent quantum dots, protein self-assembly, synergistic cancer therapy

Received: March 9, 2023
Revised: April 24, 2023
Published online:

[1] H. Sung, J. Ferlay, R. L. Siegel, M. Laversanne, I. Soerjomataram, A. Jemal, F. Bray, *Ca-Cancer J. Clin.* **2021**, *71*, 209.
[2] N. A. Jackson, J. Barrueco, R. Soufi-Mahjoubi, J. Marshall, E. Mitchell, X. Zhang, J. Meyerhardt, *Cancer* **2009**, *115*, 2617.
[3] K. K. Ciombor, C. Wu, R. M. Goldberg, *Annu. Rev. Med.* **2015**, *66*, 83.
[4] N. Kwon, H. Kim, X. Li, J. Yoon, *Chem. Sci.* **2021**, *12*, 7248.
[5] K. Lu, C. He, W. Lin, *J. Am. Chem. Soc.* **2015**, *137*, 7600.
[6] X. Liang, M. Chen, P. Bhattarai, S. Hameed, Z. Dai, *ACS Nano* **2020**, *14*, 13569.
[7] S. Li, F. Yang, Y. Wang, T. Du, X. Hou, *Chem. Eng. J.* **2023**, *451*, 138621.
[8] P. Agostinis, K. Berg, K. A. Cengel, T. H. Foster, A. W. Girotti, S. O. Gollnick, S. M. Hahn, M. R. Hamblin, A. Juzeniene, D. Kessel, M. Korbelik, J. Moan, P. Mroz, D. Nowis, J. Piette, B. C. Wilson, J. Golab, *Ca-Cancer J. Clin.* **2011**, *61*, 250.
[9] P. Hou, P. Shi, T. Jiang, H. Yin, S. Chu, M. Shi, J. Bai, J. Song, *Br. J. Cancer* **2020**, *122*, 668.
[10] Z. Shen, J. Xia, Q. Ma, W. Zhu, Z. Gao, S. Han, Y. Liang, J. Cao, Y. Sun, *Theranostics* **2020**, *10*, 9132.
[11] J. Wu, P. Shen, X. Qin, Y. Yang, C. Lin, X. Li, W. Geng, P. Gao, L. Chen, L. Miao, Y. Jiao, B. Tao, *Chem. Eng. J.* **2023**, *459*, 141507.
[12] X. Li, N. Kwon, T. Guo, Z. Liu, J. Yoon, *Angew. Chem., Int. Ed.* **2018**, *57*, 11522.
[13] Y. Deng, P. Song, X. Chen, Y. Huang, L. Hong, Q. Jin, J. Ji, *ACS Nano* **2020**, *14*, 9711.
[14] L. Gong, Y. Zhang, J. Zhao, Y. Zhang, K. Tu, L. Jiao, Q. Xu, M. Zhang, S. Han, *Small* **2022**, *18*, 2107656.
[15] Z. Meng, X. Zhou, J. Xu, X. Han, Z. Dong, H. Wang, Y. Zhang, J. She, L. Xu, C. Wang, Z. Liu, *Adv. Mater.* **2019**, *31*, 1900927.
[16] H. Wang, Y. Chao, J. Liu, W. Zhu, G. Wang, L. Xu, Z. Liu, *Biomaterials* **2018**, *181*, 310.
[17] J. Zhu, X. Wang, D. Yang, X. Song, B. Li, W. Wang, X. Dong, *Adv. Ther.* **2021**, *4*, 2100052.
[18] S. Mörikofer-Zwez, J. P. von Wartburg, H. Aebi, *Experientia* **1970**, *26*, 945.
[19] L. Góth, *Enzyme* **1989**, *41*, 191.
[20] Z.-G. Wang, S.-L. Liu, D.-W. Pang, *Acc. Chem. Res.* **2021**, *54*, 2991.
[21] C. Ding, Y. Huang, Z. Shen, X. Chen, *Adv. Mater.* **2021**, *33*, 2007768.
[22] S. Ling, X. Yang, C. Li, Y. Zhang, H. Yang, G. Chen, Q. Wang, *Angew. Chem., Int. Ed.* **2020**, *59*, 7219.
[23] C. Ding, X. Cao, C. Zhang, T. He, N. Hua, Y. Xian, *Nanoscale* **2017**, *9*, 14031.
[24] J. Gao, C. Wu, D. Deng, P. Wu, C. Cai, *Adv. Healthcare Mater.* **2016**, *5*, 2437.
[25] M. Gao, H. Zhao, Z. Wang, Y. Zhao, X. Zou, L. Sun, *Adv. Powder Technol.* **2021**, *32*, 1972.
[26] M. Zhang, R. Zhang, Y. Dong, J. Liu, Z. Gao, X. Zhou, J. Cao, *Chem. Eng. J.* **2023**, *459*, 141484.
[27] L. Yang, Y. Zhu, L. Liang, C. Wang, X. Ning, X. Feng, *Nano Lett.* **2022**, *22*, 4207.
[28] Y. Zhang, Y. Cheng, F. Yang, Z. Yuan, W. Wei, H. Lu, H. Dong, X. Zhang, *Nano Today* **2020**, *34*, 100919.
[29] S. Li, W. Zhang, H. Xue, R. Xing, X. Yan, *Chem. Sci.* **2020**, *11*, 8644.
[30] Q. Luo, C. Hou, Y. Bai, R. Wang, J. Liu, *Chem. Rev.* **2016**, *116*, 13571.
[31] L. Zhao, H. Zou, H. Zhang, H. Sun, T. Wang, T. Pan, X. Li, Y. Bai, S. Qiao, Q. Luo, J. Xu, C. Hou, J. Liu, *ACS Nano* **2017**, *11*, 938.
[32] N. Jiang, Z. Zhou, W. Xiong, J. Chen, J. Shen, R. Li, R. Ye, *Chin. Chem. Lett.* **2021**, *32*, 3948.

[33] W. He, J. Yan, F. Sui, S. Wang, X. Su, Y. Qu, Q. Yang, H. Guo, M. Ji, W. Lu, Y. Shao, P. Hou, *ACS Nano* **2018**, *12*, 11664.
[34] L. Zhao, Y. Xing, R. Wang, F. Yu, F. Yu, *ACS Appl Bio Mater* **2020**, *3*, 86.
[35] S. Zhang, *Nat. Biotechnol.* **2003**, *21*, 1171.
[36] L. Miao, J. Han, H. Zhang, L. Zhao, C. Si, X. Zhang, C. Hou, Q. Luo, J. Xu, J. Liu, *ACS Nano* **2014**, *8*, 3743.
[37] T. Wen, H. Zhang, Y. Chong, W. G. Wamer, J.-J. Yin, X. Wu, *Nano Res.* **2016**, *9*, 1663.